Energy landscape and band-structure tuning in realistic $MoS_2/MoSe_2$ heterostructures

Gabriel C. Constantinescu* and Nicholas D. M. Hine†
TCM Group, Cavendish Laboratory, University of Cambridge,
19 JJ Thomson Avenue, Cambridge CB3 0HE, UK
(Dated: April 10, 2015)

While monolayer forms of 2D materials are well-characterised both experimentally and theoretically, properties of bilayer heterostructures are not nearly so well-known. We employ high-accuracy linear-scaling DFT calculations utilising non-local van-der-Waals functionals to explore the possible constructions of the $MoS_2/MoSe_2$ interface. Utilising large supercells, we vary rotation, translation and separation of the layers without introducing unrealistic strain. The energy landscape shows very low variations under rotation, with no strongly preferred alignments. By unfolding the spectral function into the primitive cells, we show that the monolayers are more independent than in homo-bilayers, and that the electronic bandstructure of each layer is tunable through rotation, thus influencing hole effective masses.

I. INTRODUCTION

In the decade since graphene first gained prominence[1], research on layered materials has broadened significantly in scope as well as scale, as alternative materials have attracted significant interest. The most notable are transition metal dichalcogenides (TMDCs), with MoS_2 being the most prominent member. Due to increased electron mobility, elasticity, and a large direct gap, MoS_2 monolayers have applications in semiconductor electronics[2–5] and optoelectronics[6–8]. Spin-orbit coupling in odd-numbered multilayers is also proving useful for spintronics[9–12]. Moreover, the weak van-der-Waals interlayer interaction permits the simple production (through liquid or chemical exfoliation[13,14]) of few-layered and monolayered forms.

However, multilayered semiconducting TMDCs lose the direct-gap character of the monolayer[15]. In the effort to maintain monolayer properties in multilayered forms, heterostructures combining different layered materials are considered. Moreover, they hold the promise of a fine-grained selection of desired properties by simply selecting the composition[16].

Twisted graphene bilayers[17] and heterostructures between graphene and SiC[18–20] or metals[21,22] have already been successfully studied, while misoriented TMDC bilayers[23] and heterostackings have just started delivering novel theoretical[24–26] and experimental[27–31] findings. At the same time, modern fabrication techniques enable the preferential stacking of flakes through "dry transfer"[28,30] or chemical vapor deposition[32].

However, there are serious hurdles to the theoretical study of van-der-Waals heterostructures, which have held back progress in this field. Firstly, the description of the van-der-Waals interaction is beyond the abilities of traditional density functional theory (DFT). Secondly, the Moiré patterns occurring in such interfaces[26,33] can only be simulated through very large supercells. While traditional DFT has previously been used to simulate

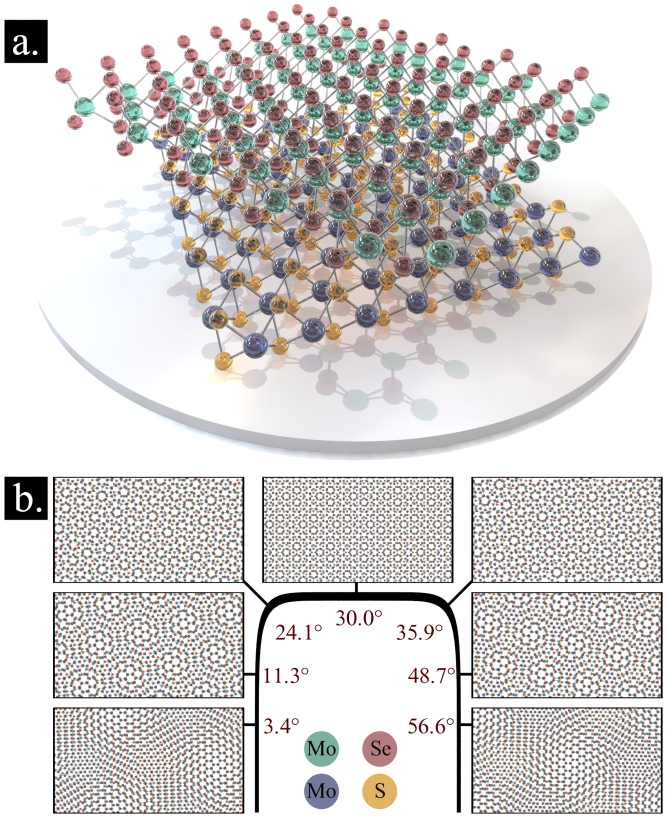

FIG. 1. (a) Example of a stacked MoS_2 / $MoSe_2$ heterostructure. (b) Moiré patterns for different angles.

large Moiré patterns[19,22], the large computational cost has prevented a thorough exploration of the configuration space.

For this reason, theoretical studies have restricted their attention to a small number of configurations[19,22,25,26], assumed high strains to reduce the cell size[34] or used empirical van-der-Waals descriptions[26].

In this work we attempt to remedy these hurdles by combining an approach enabling accurate and realistic description of the phase-space associated with TMDC heterostructures, with an accurate description of the van-der-Waals interlayer interaction. We use stacked monolayer forms (Fig. 1(a)) of molybdenum disulfide (MoS_2) with molybdenum diselenide ($MoSe_2$), as a prototype for lattice mismatched heterostructures. We perform a full scan of the associated structural parameters, i.e. rotations, interlayer spacings and translations were considered. We report three main findings: the relatively invariant energy landscape would permit virtually any interlayer angle, the band-structure of each layer is tunable through rotations, and the monolayers act more independently than in homo-bilayers. The first two results imply that heterostructured flakes can be grown with various orientations through chemical vapour deposition, each flake having slightly different bandstructure characteristics depending on the angle. This is a scalable alternative to direct-transfer techniques. The last finding shows that one can maintain, to a certain degree, the monolayer direct-gap behaviour in heterostructured multilayers, thus enhancing the photodetection and light-harvesting capabilities of few-layered stacks. The reduced interlayer interactions could also be beneficial to layered superconductors, possibly extending 2D confinement effects[35,36] to thicker stacks. More importantly, we can extend our conclusions to a whole class of semiconducting type-II layered heterostructures.

II. ENERGY LANDSCAPE

A. Methodology

1. $MoS_2/MoSe_2$

We employ linear-scaling density functional theory (LS-DFT) as implemented in the ONETEP code[37], which has been shown to display tunable accuracy equivalent to traditional plane-wave DFT calculations[38], as opposed to other large-scale methods. Traditional methods can access large system sizes at very high computational cost[22], but linear-scaling behaviour allows for an extensive scan of the $MoS_2/MoSe_2$ configuration space.

Furthermore, we use non-local van-der-Waals functionals based on the work of Dion et al.[39]. These describe the long-range charge density interactions in an ab-initio manner, avoiding the empirically-parametrised interatomic coefficients used in dispersion-corrected DFT[40]. LS-DFT as implemented in ONETEP utilizes a basis of periodic sinc functions on a real-space grid[37], with spacing controlled by a cutoff energy. Localized orbitals constructed from this basis are self-consistently optimized in-situ, eliminating basis set superposition errors[41] and the need for large basis sets; these local orbitals are termed non-orthogonal Wannier functions (NGWFs). The density kernel is also self-consistently optimised so as to minimise the total energy subject to constraints of idempotency and normalisation[42].

We chose a cutoff energy of 800 eV and employ the PAW formalism[43] with the GBRV atomic datasets[44]. For the chalcogen and transition metal atoms, the outermost 6 and 14 electrons were retained as valence, resulting in four and 13 NGWFs per atom, respectively. All NGWFs have a localisation radius of 13.0 Bohr.

We will predominantly use the optB88-vdW exchange-correlation (XC) functional[45] as it reproduces well the bulk lattice parameters of MoS_2 (Table I in SM). The optimised in-plane lattice vectors for the monolayer MoS_2 and $MoSe_2$ were 3.19 Å and 3.32 Å, in agreement with other theoretical[46] and experimental sources[47,48]. Since the LS-DFT calculations were performed at the Γ point, the supercell size is equivalent to the number of primitive-cell k-points in traditional methods. To obtain good convergence we considered structures containing at least 144 MoS_2 formula units (Table II in SM). Thus, the number of atoms in our $MoS_2/MoSe_2$ supercells ranges from 831 to 1872 (Table III in SM).

The large unit cells required were constructed according to the specifications of K. Hermann[49]. A maximum strain of 1% in the $MoSe_2$ layer results in manageable supercell sizes, while not affecting the $MoSe_2$ electronic properties[50–52]. Interlayer rotations in the range $0° - 60°$ fully describe twisting, due to the three-fold rotational symmetry, with reflection symmetry around 60°.

2. *Twisted MoS_2*

In addition, to measure the effect of rotation in homostructural constructions, we also consider the case of twisted MoS_2 bilayers. As opposed to $MoS_2/MoSe_2$, the Moire coincidence cells are small in this case (maximum 78 atoms), allowing us to perform traditional plane-wave DFT calculations using QuantumEspresso[53]. The k-space sampling of each of the supercells was adapted such that it would be equivalent to at least a 12×12 sampling of the MoS_2 monolayers. We considered a 800 eV plane-wave kinetic energy cutoff, the GBRV USPP atomic datasets and a cell height of 30.0 Å, in order to avoid spurious interaction between bilayer replicas. All the MoS_2 bilayer calculations were performed at the interlayer distance found in the MoS_2 bilayer with bulk stacking, i.e. 6.25 Å.

Two initial configurations were considered: (I) – starting from the MoS_2 bulk stacking (i.e. antialigned MoS_2 units), we rotate the top layer using a Mo atom as the center; (II) – we translate the top layer in configuration I by a Mo-S bond length along the Mo-S bond direction, and repeat the procedure.

B. Twisted MoS_2 bilayers

The obtained interlayer binding energies are shown in Table I and the structures are shown in Fig. 2. Configurations (I) and (II) correspond to the 0.0° cases of Fig. 2(a) and Fig. 2(b), respectively.

TABLE I. Binding energy (meV/bottom MoS_2-unit) for twisted MoS_2 bilayers.

Angle [°]	case (I)	case (II)
0.0	-220.1	-207.3
21.8	-172.2	-172.3
27.8	-172.4	-172.4
32.2	-172.4	-172.4
38.2	-172.2	-172.3
60.0	-219.0	-65.9

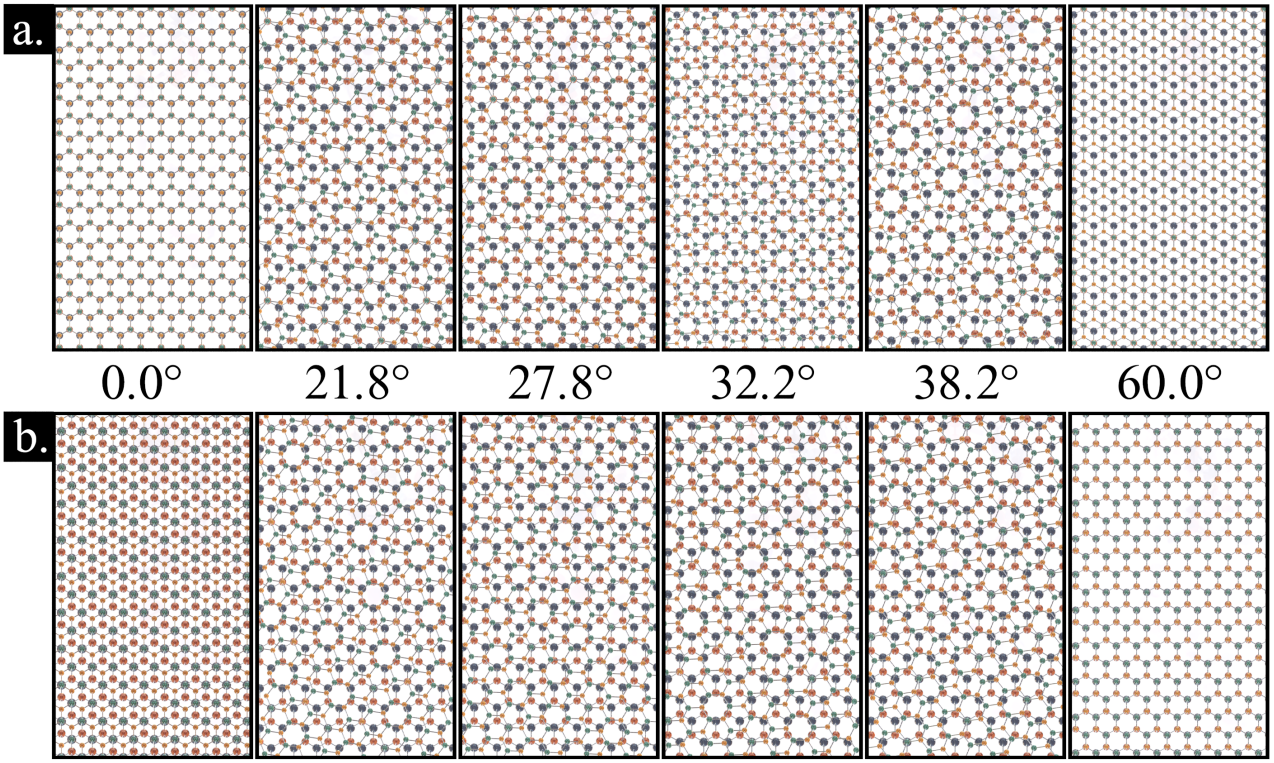

FIG. 2. Twisted MoS_2 structures, starting from configuration (I)– (a) and (II)–(b). The corresponding relative angles are shown between the inset rows. The top (bottom) Mo is light (dark) blue, while the S from the top (bottom) monolayer is yellow (red).

From Table I, it is obvious that apart from the 0° and 60° cases, the energy variation associated with the rotation of

the layers is negligible. The high-coupling and binding-energy variations at 0° and 60° occur due to spontaneous coherence between the layers, given by the alignment of identical lattice vectors, as we shall prove later in the article.

This behaviour is also in good agreement with the work of Castellanos-Gomez et al.[54], which employed Raman spectroscopy to show reduced interlayer coupling in folded MoS_2 layers. Therefore, energetic decoupling between misaligned monolayers is experimentally implied.

Moreover, it appears that translation does not have any effect on the energy landscape of twisted MoS_2 bilayers, once one has left the high-coupling angles. On the other hand, we shall later prove that in $MoS_2/MoSe_2$ such high coupling cases are not present, as the lattice vectors lengths of the two monolayers are different. This implies that there is no need to explicitly consider translations in $MoS_2/MoSe_2$ interfaces.

C. $MoS_2/MoSe_2$ heterostructures

1. *LS-DFT approach*

The large $MoS_2/MoSe_2$ coincidence cells and differing lattice constants determine a continuously varying stacking order throughout the heterostructures (Fig. 1(b)). This, along with our previous proof that translations produce negligible energy differences in rotated bilayers (Table I), suggests that there is no need to consider explicit lateral translations for $MoS_2/MoSe_2$. Therefore, to investigate the structural stability of such heterostructures, we only need to rotate the $MoSe_2$ layer on top of the MoS_2 layer, while also varying the interlayer distance.

The variation of binding energy with interlayer distance d (the distance between the Mo-planes) is shown in Fig. 3(a). Its optimal value varies in the range $6.65 - 6.70$ Å for different rotation angles. Komsa et al.[25]) reported a similar value for the 16.1° case. We attribute this rather constant behaviour to steric effects induced by the continuous change in stacking throughout the structures. The same effect was reported in twisted MoS_2 bilayers by van-der-Zande et al.[23], where the variation in interlayer distance with angle is less than 0.1 Å, for cases other than 0° and 60°. As shown further, for monolayers with different lattice constants there are no such special angles. Thus, we henceforth fix the interlayer distance to 6.70 Å.

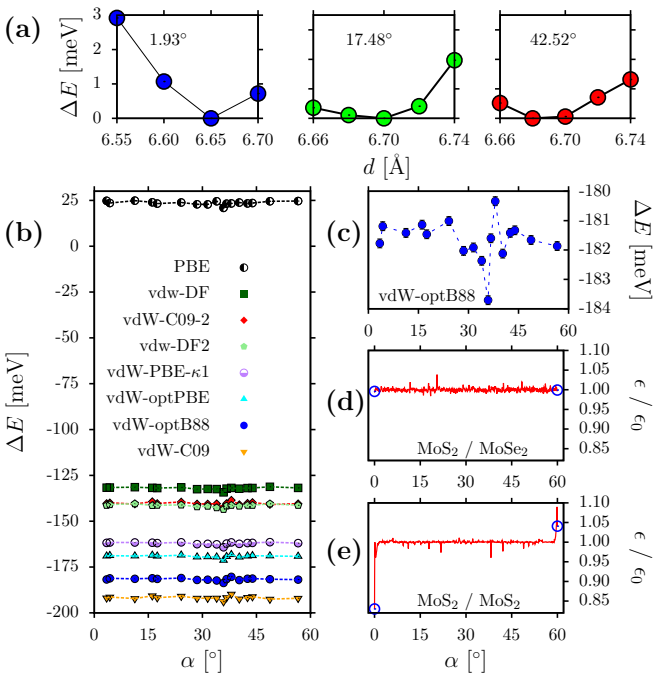

FIG. 3. (a) Interlayer distance optimisation, with the most stable positions taken as energy reference. (b) Interaction energies for different XC functionals (at fixed charge density obtained with optB88-vdW). (c) Binding energies obtained self-consistently with optB88-vdW. (d) Local density-potential interaction model for the $MoS_2/MoSe_2$ heterostructures and (e) MoS_2 bilayers. Values at 0° and 60° are marked with blue circles. All reported energy values are per MoS_2 formula unit.

We next perform binding energy calculations using LS-DFT with optB88-vdW, for a wide range of angles. The obtained binding energies are shown in Fig. 3(c). The energy surface variation appears to be only 4 meV/MoS_2 – unit, a value at the edge of DFT accuracy and irrelevant in thermally elevated conditions. The error bar accounts for the possible energy variations due to changes in the sampling grid orientation (details in SM).

While the rotationally-dependent energy landscape appears irregular, in contrast to the smooth landscape associated with general interlayer translations[55], the absolute variations are actually very low. This reduced scale is even more clear when it is compared to the absolute binding energies obtained by utilising different XC functionals and non-local vdW descriptions. These are applied to the density determined self-consistently with optB88-vdW (Fig. 3(b)). The fact that the shape and magnitude of the energy variation are maintained indicates that the only role of the vdW component is to rigidly shift the absolute binding energy[55].

Therefore, it is clear that the apparent irregularity and low overall variation of the energy landscape is not of dispersive nature, but has a purely electrostatic origin.

2. Perturbative approach

We can prove this statement through arguments similar to those proposed for twisted graphene bilayers[17,56]. We consider a simple perturbation-theory model, in which the binding energy derives from a local density-potential interaction:

$$\epsilon = \int \rho_1(\mathbf{r}) V_2(\mathbf{r})\ \mathrm{d}\mathbf{r} + \int \rho_2(\mathbf{r}) V_1(\mathbf{r})\ \mathrm{d}\mathbf{r} \propto \sum_{\mathbf{G}_1,\mathbf{G}_2} \left[\tilde{\rho}_1(\mathbf{G}_1)\tilde{V}_2^*(\mathbf{G}_2) + \tilde{\rho}_2^*(\mathbf{G}_2)\tilde{V}_1(\mathbf{G}_1)\right]\delta_{\mathbf{G}_1,\mathbf{G}_2}\ , \tag{1}$$

where $\rho_i(\mathbf{r})$ is the charge density of the independent monolayer i and $V_i(\mathbf{r})$ contains only the local parts of the pseudo, Hartree, vdW and XC potentials. $\mathbf{G}_2$ is rotated as the $MoSe_2$ layer is rotated. In reciprocal space we only need to consider a finite region of the momentum-space, due to the kinetic energy cutoff of the underlying grid. The Kronecker delta in Eq. 2 is replaced by a Gaussian with a broadening of 0.02 Å^{-1}, equivalent to $\approx 1\%$ of the $MoSe_2$ monolayer reciprocal lattice vector. A baseline energy ϵ_0 is defined by considering the sum in Eq. 2 only for $\mathbf{G}_1, \mathbf{G}_2$ with zero in-plane components, as these vectors are invariant under rotation. Therefore, this simple model offers some insight into the relative binding energy variation under interlayer rotation. The results are shown in Fig. 3(d). The same approach is also applied to twisted MoS_2 bilayers (Fig. 3(e)).

In the case of $MoS_2/MoSe_2$, ϵ shows an apparently irregular, but consistently low variation, of maximum 0.06 ϵ_0. The difference between the aforementioned case and the twisted MoS_2 bilayer lies in the large variation of ϵ near 0° and 60°. From Eq. 2, it is clear that for those angles, momentum-matching occurs in the MoS_2 bilayers, as the reciprocal lattice vectors have identical lengths. Traditional DFT calculations on twisted MoS_2 bilayers (Table I) confirm that significant energy variations occur only for 0° and 60°. Therefore, while in MoS_2 bilayers interlayer decoupling occurs due to rotations away from high-symmetry configurations, in $MoS_2/MoSe_2$ heterostructures the decoupling is caused by the differing lattice parameters. Thus, in $MoS_2/MoSe_2$ there will not be any high-interaction angles as observed in MoS_2 bilayers.

In order to connect this model with the actual LS-DFT calculations, we can relate the baseline ϵ_0 to the average local part of the interaction energy $\overline{\Delta E_\mathrm{L}}$, obtained from the LS-DFT binding energy (Fig. 3(c)) by removing the non-local vdW contribution:

$$\Delta E_\mathrm{L} = \Delta E - (E_\mathrm{nl}^{(\mathrm{T})} - E_\mathrm{nl}^{(1)} - E_\mathrm{nl}^{(2)})\ , \tag{2}$$

where ΔE is the calculated LS-DFT binding energy, ΔE_L is the local part of the LS-DFT binding energy and $E_\mathrm{nl}^{(\mathrm{T})}$, $E_\mathrm{nl}^{(1)}$ and $E_\mathrm{nl}^{(2)}$ are the non-local vdW energy contributions for the complete heterostructure, and the independent monolayers, respectively.

From the LS-DFT calculations, we obtain $\overline{\Delta E_\mathrm{L}} = 106.3$ meV / MoS_2-unit. Thus, considering that the model ϵ shows a maximum variation of $0.06\epsilon_0$, we should expect a maximum variation of $0.06\ \overline{\Delta E_\mathrm{L}} = 6.4$ meV / MoS_2-unit, a value comparable with the actual variation observed in the LS-DFT calculations. This estimate is an upper bound, as smaller broadening factors further restrict the momentum-matching condition. Therefore, the variation of the interlayer interaction energy is limited to only a few meV per MoS_2 formula unit, due to the momentum mismatch (Eq. 1) caused by the differing in-plane lattice vectors of MoS_2 and $MoSe_2$. We expect the same behaviour in any lattice-mismatched layered system, as long as the difference in lattice parameters is large enough to prevent the alignment between the monolayers. For the former case MoS_2/WSe_2 is an immediate candidate, as WSe_2 has almost identical lattice parameters to $MoSe_2$[46], while MoS_2/WS_2 exemplifies the latter case[57]. Therefore, by growing heterostructures with significant lattice mismatch, one would obtain flakes showing various angles between the substrate and overlayer, structures which could then be selected preferentially.

III. ELECTRONIC STRUCTURE

A. Methodology

We next investigate the electronic structure of a monolayer in the presence of the weak external perturbation from the other layer. We argue that the bandstructure of the whole supercell is not a useful concept for such large cells, as it is not intuitive how electronic effects unfold to the Brillouin zone (BZ) of each monolayer. To solve this problem, we unfold the single-particle supercell spectral function by projecting it onto the monolayer of interest

and changing the representation basis to the primitive-cell eigenstates of this monolayer. Similar BZ unfolding procedures have been successfully used on heterostructures in the past[18], and provide a benchmark for future experimental studies[58]. We have employed a method based on that of C.C. Lee et al.[59], and have adapted it to the PAW and NGWF formalisms. Thus, we gain means of direct comparison with angular-resolved photoemission spectroscopy experiments.

We enforce the NGWFs to have the translational symmetry of the stoichiometric units by optimising the NGWFs for each individual monolayer. The two sets of NGWFs are then combined in a heterostructure calculation, where only the density kernel is self-consistently optimised. By diagonalising the KS Hamiltonian, one obtains the eigenstates for the combined system.

The general idea of the unfolding is the following:

$$A^I_{\mathbf{k}j,\mathbf{k}j} = \sum_{\substack{\mathbf{K},\\ \rho\in I}} \langle \Psi_{\mathbf{k}j}|\Psi_{\mathbf{K}J}\rangle \, A_{\mathbf{K}J,\mathbf{K}J} \, \langle \Psi_{\mathbf{K}J}|\phi^\rho\rangle \, \langle \phi_\rho|\Psi_{\mathbf{k}j}\rangle \tag{3}$$

$A^I_{\mathbf{k}j,\mathbf{k}j}$ is the spectral function projected on monolayer I in the representation of the primitive cell eigenstates $|\Psi_{\mathbf{k}j}\rangle$, $A_{\mathbf{K}J,\mathbf{K}J}$ is the heterostructure spectral function for the supercell eigenstates $|\Psi_{\mathbf{K}J}\rangle$ and $\sum_{\rho\in I}|\phi^\rho\rangle\langle\phi_\rho|$ projects onto the NGWFs of subsystem I. Full derivations can be found in SM.

B. Spectral function unfolding

We first examine the 30° rotation case, as shown in Fig. 4(a). We compare the unfolded spectral weight of each interacting monolayer with its uninfluenced counterpart. Firstly, it is clear that the pristine monolayer MoS_2 bandstructure is in good agreement with experimental ARPES data[58]. It is well known that the MoS_2 monolayer has a direct $K-K$ gap, which we also observe. While the highest VB at Γ is close to that at K, the difference is within the accuracy of DFT bandstructure calculations.

We note low spectral-weight intrusions from $MoSe_2$ into MoS_2 and vice-versa only near Γ, with minimal change elsewhere in the BZ. The localisation of the interaction near the BZ origin is due to the momentum-mismatch: as proven by Eq. 1, the interlayer interaction is rotationally invariant only at $\mathbf{G}_{1_{||}} = \mathbf{G}_{2_{||}} = \mathbf{0}$. This momentum-space localisation of the electronic interaction is in agreement with other theoretical works[25,26], and based on our previous argument we expect identical effects in general

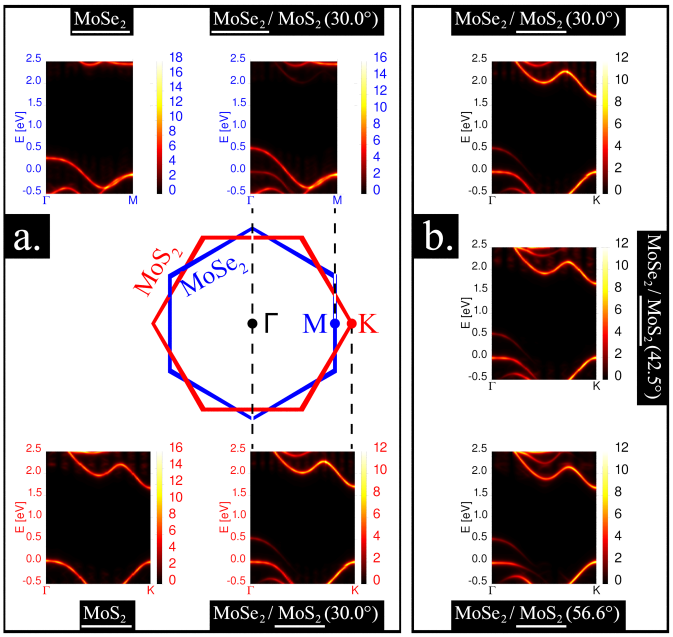

FIG. 4. Spectral function in the representation of the primitive-cell monolayer eigenstates. (a) Projection on individual monolayers for the 30° case: $MoSe_2$ (top), MoS_2 (bottom), and schematic of overlapping monolayer Brillouin-zones (center). Angle dependence of the MoS_2-projected spectral function (b). The energy of the highest valence band (VB) at K for the interacting MoS_2 is taken as reference.

lattice mismatched layered heterostructures. Such hybridisation of $MoS_2/MoSe_2$ bands near Γ indicates the significance of interlayer recombination effects, as observed experimentally in MoS_2/WSe_2[29,33]. Moreover, it appears that the highest VB at Γ for $MoSe_2$ is repelled (by ≈ 0.2 eV) due to the intruding MoS_2 band, the hole effective mass decreasing in the process. Fortunate band alignment allows the originally highest VB at Γ in MoS_2 to remain at the same energy.

The intrusion of $MoSe_2$ bands near Γ in the MoS_2 transforms the latter into an indirect $\Gamma-K$ gap semiconductor. However, the low spectral weight of this new VB band at Γ indicates a low associated transition probability. This behaviour differs from the well-known MoS_2 bilayer case[58], where there are two split bands at Γ both with significant spectral weight. Therefore, as opposed to homo-stackings, this heterostructure will show improved behaviour in processes requiring a direct band gap, as proven by the significant photoluminescence response observed in $MoS_2/MoSe_2$ interfaces[60] and photoluminescence quenching in MoS_2 bilayers[6]. This in-

creased layer independence is not general, as experimental MoS_2/WSe_2 heterstructures show significantly enhanced interlayer electronic coupling[33,61].

Finally, we analyse the effects of rotation on $A^{MoS_2}_{\mathbf{k}j,\mathbf{k}j}$, as shown in Fig. 4(b). It is clear that the curvature of the original highest VB at the Γ point varies with the rotation angle. Using a simple parabolic fit for the visible part of the aforementioned band, we calculated the effective hole mass in the pristine MoS_2 monolayer to be 3.19 m_0, a value roughly comparable to other reported theoretical[62] (2.8 m_0) and experimental[58] ((2.4±0.3) m_0) results, where m_0 is the electron mass. However, for the rotated structures, the hole effective masses at Γ for the same band as before were calculated to be 2.64 m_0 for 30.0°, 3.15 m_0 for 42.5°, and 6.11 m_0 for 56.6°. Recent experiments[63] also confirm the possibility of bandstructure curvature tuning in 2D heterostructures.

This variation is due to band repelling, as the MoS_2 $\Gamma-K$ path comes in contact with a different path in the $MoSe_2$ BZ for each rotation angle. The bands near K remain unaltered by the interlayer influence, leading to no changes in the electron effective mass. Finally, the local density of states and the VB top/conduction band bottom distribution (see SM) indicate the localisation of the holes (electrons) on the $MoSe_2$ (MoS_2) layer, in agreement with experimental[60] and theoretical[26] studies.

C. Local Density of States

In this subsection, we discuss the total density of states (DOS) and local density of states (LDOS) as projected on the component monolayers in the $MoS_2/MoSe_2$ heterostructures. The results are shown in Fig. 5.

In all cases, the valence manifold near the Fermi level is almost fully occupied by states lying on the $MoSe_2$ layer, while the conduction manifold contains only MoS_2 states near the Fermi level. This is in complete agreement with the band alignment obtained from the spectral-function unfolding (Fig. 4), and also experimental sources[60], all of which indicate charge separation in the heterostructure. Thus, the holes are mostly on the $MoSe_2$, while the electrons are in the MoS_2, a behaviour specific to type II heterostructures.

We remind the reader that in Fig. 4 we have observed a band of low spectral weight which is protruding in the MoS_2 layer of the heterostructure, transforming it in an indirect-gap semiconductor. The LDOS projections confirm that the aforementioned band has almost negligible

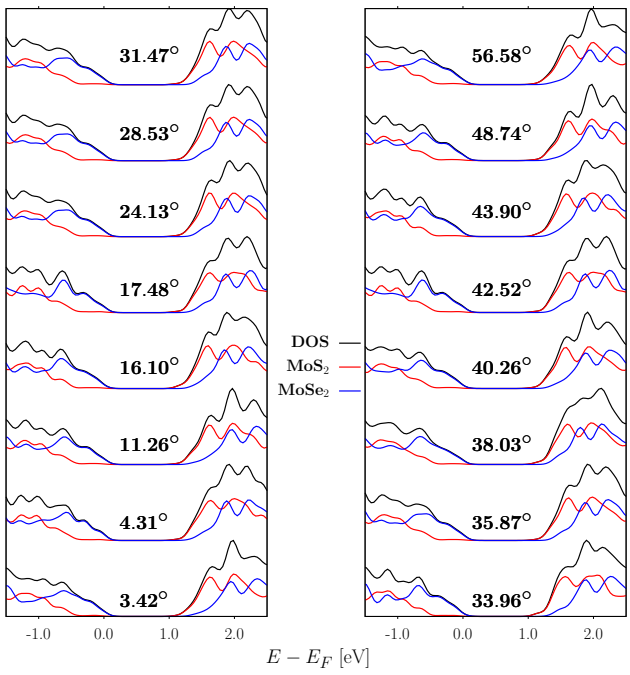

FIG. 5. DOS (black lines) and LDOS (red lines for MoS_2 layer, blue lines for $MoSe_2$ layer) for $MoS_2/MoSe_2$ heterostructures. The Fermi level is taken as reference.

weight, as the contribution of the MoS_2 layer to the valence manifold close to the Fermi level is almost negligible.

In regards to the angle dependence, the variations in the DOS and LDOS are low in the vicinity of the Fermi level, the only notable difference being a valley in the $MoSe_2$ LDOS around −0.50 eV. This appears to be enhanced at selected angles (17.48°, 42.52°), indicating that the bandstructure is indeed slightly tunable.

IV. CONCLUSIONS

In conclusion, we have shown that in the $MoS_2/MoSe_2$ heterostructure there is a relative invariance of the interlayer binding energy under rotation. Because this depends only on the lattice mismatch and not on the atomistic detail of the structure, similar behaviour is to be expected for other lattice mismatched heterostructures. By projecting the supercell spectral function into the primitive cell, we have shown that the band intrusions are of low spectral weight, implying that the layers of these heterostructures are more independent than in the corresponding homo-stacks. Lastly, due to band repulsion and hybridisation, the bandstructure near the Brillouin-zone

center of each layer is tunable, allowing the variation of the hole effective masses.

ACKNOWLEDGMENTS

The authors acknowledge the support of the Winton Programme for the Physics of Sustainability. Computing resources were provided by the Darwin Supercomputer of the University of Cambridge High Performance Computing Service and the Argonne Leadership Computing Facility at Argonne National Laboratory, supported by the Office of Science of the U.S. Department of Energy under contract DE-AC02-06CH11357. GCC acknowledges the support of the Cambridge Home and EU Scholarship Scheme.

* gcc32@cam.ac.uk
† ndmh3@cam.ac.uk

[1] K. S. Novoselov, D. Jiang, F. Schedin, T. J. Booth, V. V. Khotkevich, S. V. Morozov, and A. K. Geim, PNAS **102**, 10451 (2005).
[2] Y. Yoon, K. Ganapathi, and S. Salahuddin, Nano Lett. **11**, 3768 (2011).
[3] B. Radisavljevic, A. Radenovic, J. Brivio, V. Giacometti, and A. Kis, Nat Nano **6**, 147 (2011).
[4] B. Radisavljevic, M. B. Whitwick, and A. Kis, ACS Nano **5**, 9934 (2011).
[5] Y. Zhang, J. Ye, Y. Matsuhashi, and Y. Iwasa, Nano Lett. **12**, 1136 (2012).
[6] A. Splendiani, L. Sun, Y. Zhang, T. Li, J. Kim, C.-Y. Chim, G. Galli, and F. Wang, Nano Lett. **10**, 1271 (2010).
[7] G. Eda, H. Yamaguchi, D. Voiry, T. Fujita, M. Chen, and M. Chhowalla, Nano Lett. **11**, 5111 (2011).
[8] Z. Yin, H. Li, H. Li, L. Jiang, Y. Shi, Y. Sun, G. Lu, Q. Zhang, X. Chen, and H. Zhang, ACS Nano **6**, 74 (2012).
[9] K. F. Mak, K. He, J. Shan, and T. F. Heinz, Nat Nano **7**, 494 (2012).
[10] H. Zeng, J. Dai, W. Yao, D. Xiao, and X. Cui, Nat Nano **7**, 490 (2012).
[11] T. Cao, G. Wang, W. Han, H. Ye, C. Zhu, J. Shi, Q. Niu, P. Tan, E. Wang, B. Liu, et al., Nat Commun **3**, 887 (2012).
[12] R. Suzuki, M. Sakano, Y. J. Zhang, R. Akashi, D. Morikawa, A. Harasawa, K. Yaji, K. Kuroda, K. Miyamoto, T. Okuda, et al., Nat Nano **9**, 611 (2014).
[13] J. N. Coleman, M. Lotya, A. ONeill, S. D. Bergin, P. J. King, U. Khan, K. Young, A. Gaucher, S. De, R. J. Smith, et al., Science **331**, 568 (2011).
[14] Q. H. Wang, K. Kalantar-Zadeh, A. Kis, J. N. Coleman, and M. S. Strano, Nat. Nano. **7**, 699 (2012).
[15] A. Kuc, N. Zibouche, and T. Heine, Phys. Rev. B **83**, 245213 (2011).
[16] A. K. Geim and I. V. Grigorieva, Nature **499**, 419 (2013).
[17] S. Shallcross, S. Sharma, and O. A. Pankratov, Phys. Rev. Lett. **101**, 056803 (2008).
[18] S. Kim, J. Ihm, H. Choi, and Y.-W. Son, Phys. Rev. Lett. **100**, 176802 (2008).
[19] Y. Qi, S. Rhim, G. Sun, M. Weinert, and L. Li, Phys. Rev. Lett. **105**, 085502 (2010).
[20] J. Hass, F. Varchon, J. Milln-Otoya, M. Sprinkle, N. Sharma, W. de Heer, C. Berger, P. First, L. Magaud, and E. Conrad, Phys. Rev. Lett. **100**, 125504 (2008).
[21] A. Varykhalov, J. Sánchez-Barriga, A. Shikin, C. Biswas, E. Vescovo, A. Rybkin, D. Marchenko, and O. Rader, Phys. Rev. Lett. **101**, 157601 (2008).
[22] M. Iannuzzi, I. Kalichava, H. Ma, S. Leake, H. Zhou, G. Li, Y. Zhang, O. Bunk, H. Gao, J. Hutter, et al., Phys. Rev. B **88**, 125433 (2013).
[23] A. M. van der Zande, J. Kunstmann, A. Chernikov, D. A. Chenet, Y. You, X. Zhang, P. Y. Huang, T. C. Berkelbach, L. Wang, F. Zhang, et al., Nano Lett. **14**, 3869 (2014).
[24] K. Kośmider and J. Fernández-Rossier, Phys. Rev. B **87**, 075451 (2013).
[25] H.-P. Komsa and A. V. Krasheninnikov, Phys. Rev. B **88**, 085318 (2013).
[26] J. Kang, J. Li, S.-S. Li, J.-B. Xia, and L.-W. Wang, Nano Lett. **13**, 5485 (2013).
[27] M. Bernardi, M. Palummo, and J. C. Grossman, Nano Lett. **13**, 3664 (2013).
[28] L. Britnell, R. M. Ribeiro, A. Eckmann, R. Jalil, B. D. Belle, A. Mishchenko, Y.-J. Kim, R. V. Gorbachev, T. Georgiou, S. V. Morozov, et al., Science **340**, 1311 (2013).
[29] M. M. Furchi, A. Pospischil, F. Libisch, J. Burgdörfer, and T. Mueller, Nano Lett. **14**, 4785 (2014).
[30] T. Georgiou, R. Jalil, B. D. Belle, L. Britnell, R. V. Gorbachev, S. V. Morozov, Y.-J. Kim, A. Gholinia, S. J. Haigh, O. Makarovsky, et al., Nat Nano **8**, 100 (2013).
[31] C.-J. Shih, Q. H. Wang, Y. Son, Z. Jin, D. Blankschtein, and M. S. Strano, ACS Nano **8**, 5790 (2014).
[32] Y. Shi, W. Zhou, A.-Y. Lu, W. Fang, Y.-H. Lee, A. L. Hsu, S. M. Kim, K. K. Kim, H. Y. Yang, L.-J. Li, et al., Nano Lett. **12**, 2784 (2012).
[33] H. Fang, C. Battaglia, C. Carraro, S. Nemsak, B. Ozdol, J. S. Kang, H. A. Bechtel, S. B. Desai, F. Kronast, A. A. Unal, et al., PNAS p. 201405435 (2014).
[34] H. Terrones, F. López-Uras, and M. Terrones, Sci. Rep. **3** (2013).

[35] H. Jeffrey Gardner, A. Kumar, L. Yu, P. Xiong, M. P. Warusawithana, L. Wang, O. Vafek, and D. G. Schlom, Nature Physics **7**, 895 (2011).

[36] J. Biscaras, N. Bergeal, S. Hurand, C. Feuillet-Palma, A. Rastogi, R. C. Budhani, M. Grilli, S. Caprara, and J. Lesueur, Nat Mater **12**, 542 (2013).

[37] C.-K. Skylaris, P. D. Haynes, A. A. Mostofi, and M. C. Payne, J. Chem. Phys. **122**, 084119 (2005).

[38] C.-K. Skylaris and P. D. Haynes, J. Chem. Phys. **127**, 164712 (2007).

[39] M. Dion, H. Rydberg, E. Schröder, D. C. Langreth, and B. I. Lundqvist, Phys. Rev. Lett. **92**, 246401 (2004).

[40] S. Grimme, J. Chem. Phys. **124**, 034108 (2006).

[41] P. D. Haynes, C.-K. Skylaris, A. A. Mostofi, and M. C. Payne, phys. stat. sol. (b) **243**, 2489 (2006).

[42] P. D. Haynes, C. K. Skylaris, A. A. Mostofi, and M. C. Payne, J. Phys.: Condens. Matter **20**, 294207 (2008).

[43] P. E. Blöchl, Phys. Rev. B **50**, 17953 (1994).

[44] K. F. Garrity, J. W. Bennett, K. M. Rabe, and D. Vanderbilt, Comput. Mater. Sci. **81**, 446 (2014).

[45] J. Klimeš, D. R. Bowler, and A. Michaelides, J. Phys.: Condens. Matter **22**, 022201 (2010).

[46] J. Kang, S. Tongay, J. Zhou, J. Li, and J. Wu, Applied Physics Letters **102**, 012111 (2013).

[47] Y. Yu, C. Li, Y. Liu, L. Su, Y. Zhang, and L. Cao, Sci. Rep. **3** (2013).

[48] P. Joensen, R. F. Frindt, and S. R. Morrison, Materials Research Bulletin **21**, 457 (1986).

[49] K. Hermann, J. Phys.: Condens. Matter **24**, 314210 (2012).

[50] P. Johari and V. B. Shenoy, ACS Nano **6**, 5449 (2012).

[51] H. J. Conley, B. Wang, J. I. Ziegler, R. F. Haglund, S. T. Pantelides, and K. I. Bolotin, Nano Lett. **13**, 3626 (2013).

[52] M. Ghorbani-Asl, S. Borini, A. Kuc, and T. Heine, Phys. Rev. B **87**, 235434 (2013).

[53] P. Giannozzi, S. Baroni, N. Bonini, M. Calandra, R. Car, C. Cavazzoni, D. Ceresoli, G. L. Chiarotti, M. Cococcioni, I. Dabo, et al., J. Phys.: Condens. Matter **21**, 395502 (2009), ISSN 0953-8984.

[54] A. Castellanos-Gomez, H. S. J. van der Zant, and G. A. Steele, Nano Res. **7**, 1 (2014), ISSN 1998-0124, 1998-0000.

[55] G. Constantinescu, A. Kuc, and T. Heine, Phys. Rev. Lett. **111**, 036104 (2013).

[56] S. Shallcross, S. Sharma, E. Kandelaki, and O. A. Pankratov, Phys. Rev. B **81**, 165105 (2010).

[57] Y. Gong, J. Lin, X. Wang, G. Shi, S. Lei, Z. Lin, X. Zou, G. Ye, R. Vajtai, B. Yakobson, et al., Nat Mater **13**, 1135 (2014).

[58] W. Jin, P.-C. Yeh, N. Zaki, D. Zhang, J. T. Sadowski, A. Al-Mahboob, A. M. van der Zande, D. A. Chenet, J. I. Dadap, I. P. Herman, et al., Phys. Rev. Lett. **111**, 106801 (2013).

[59] C.-C. Lee, Y.-T. Yukiko, and O. Taisuke, J. Phys. Condens. Matter **25** (2013).

[60] F. Ceballos, M. Z. Bellus, H.-Y. Chiu, and H. Zhao, ACS Nano (2014).

[61] M.-H. Chiu, M.-Y. Li, W. Zhang, W.-T. Hsu, W.-H. Chang, M. Terrones, H. Terrones, , and L.-J. Li, ACS Nano **8**, 9649 (2014).

[62] H. Peelaers and C. G. Van de Walle, Phys. Rev. B **86**, 241401 (2012).

[63] H. C. Diaz, J. Avila, C. Chen, R. Addou, M. C. Asensio, , and M. Batzill, Nano Letters **15**, 1135 (2015).